Nano Energy 22 (2016) 507–513

Contents lists available at ScienceDirect

Nano Energy

journal homepage: www.elsevier.com/locate/nanoen

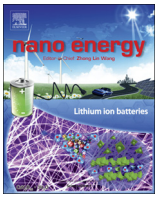

Full paper

Ruddlesden–Popper perovskite sulfides $A_3B_2S_7$: A new family of ferroelectric photovoltaic materials for the visible spectrum

Hua Wang [a], Gaoyang Gou [a,*], Ju Li [a,b,c,**]

[a] Frontier Institute of Science and Technology, and State Key Laboratory for Mechanical Behavior of Materials, Xi'an Jiaotong University, Xi'an 710049, People's Republic of China

[b] Department of Nuclear Science and Engineering, Massachusetts Institute of Technology, Cambridge, MA 02139, United States

[c] Department of Materials Science and Engineering, Massachusetts Institute of Technology, Cambridge, MA 02139, United States

ARTICLE INFO

Article history:
Received 25 August 2015
Received in revised form
16 February 2016
Accepted 16 February 2016
Available online 24 February 2016

Keywords:
Perovskite solar cells
Ferroelectric photovoltaics
First-principles calculations
Direct-bandgap optical absorption
Hybrid improper ferroelectrics

ABSTRACT

Perovskite ferroelectric materials exhibit the novel ferroelectric photovoltaic effect, where photon-excited electron–hole pairs can be separated by ferroelectric polarization. Especially, semiconducting ferroelectric materials with small band gaps (E_g) have been extensively studied for applications in solar energy conversion. Traditional route for creating semiconducting ferroelectrics requires cation doping, where E_g of the insulating perovskite ferroelectric oxides are reduced via substitution of certain cations. But cation doping tends to reduce the carrier mobility due to the scattering, and usually lead to poor photovoltaic efficiency. In the present work, based on first-principles calculations, we propose and demonstrate a new strategy for designing stoichiometric semiconducting perovskite ferroelectric materials. Specifically, we choose the parent non-polar semiconducting perovskite sulfides ABS_3 with *Pnma* symmetry, and turn them into ferroelectric Ruddlesden–Popper $A_3B_2S_7$ perovskites with spontaneous polarizations. Our predicted Ruddlesden–Popper $Ca_3Zr_2S_7$ and other derived compounds exhibit the room-temperature stable ferroelectricity, small band gaps ($E_g < 2.2$ eV) suitable for the absorption of visible light, and large visible-light absorption exceeding that of Si.

1. Introduction

Due to the unique ferroelectric–photovoltaic (FE-PV) effect, ferroelectric materials have been extensively investigated for photovoltaic applications. Unlike the traditional semiconconductor PV devices, which rely on p–n junctions to generate photocurrent, ferroelectric materials have spontaneous polarization, built-in depolarization field, and unconventional mechanisms for the separation of photo-excited electron–hole pairs [1,2]. As a result, heterogeneous p–n junctions are not required in FE–PV devices. Various ferroelectric materials, including $LiNbO_3$ single crystal [3] and $BiFeO_3$ thin films [4–9] can produce PV responses along their polarization directions. Moreover, ferroelectric materials exhibit the electric switchable PV responses [6,10] and their output photovoltages can greatly exceed E_g of the system [11]. These unique properties allow FE-PV devices to potentially have energy conversion efficiency beyond the Shockley–Queisser limit [12].

However, most ferroelectric materials known to date are perovskite oxides with large E_g above 3.3 eV. The poor absorption of the visible-light spectrum limits these ferroelectric materials for PV applications. Thus some research efforts have focused on developing effective approaches to reduce E_g of ferroelectric oxides for absorption of more visible light. Cation doping method has been widely adopted for this purpose [13–15]. After substitution of perovskite *B*-site cations by other transition metals, many semiconducting ferroelectric oxides have been created [10,16–19]. For example, a small E_g of 1.39 eV has been reported in ferroelectric $[KNbO_3]_{1-x}[BaNi_{1/2}Nb_{1/2}O_{3-\delta}]_x$ solid solutions [10]. Double perovskite Bi_2FeCrO_6 has a tunable E_g between 1.4 and 2.7 eV [19]. While cation substitution method can indeed reduce E_g of ferroelectric oxides, it will also produce structural disorder, non-stoichiometric defects or oxygen vacancies into the systems. As a result, cation-doped ferroelectric oxides usually have low carrier mobility and poor transport properties. In fact, except for very few cases [19], most cation-doped semiconducting ferroelectric oxide solid-solutions still have low output photocurrent densities on the order of $\mu A/cm^2$ and energy conversion efficiency less than 1% [1].

In our work, instead of using cation doped solid solutions, we will design and predict a new family of *stoichiometric* perovskite

* Corresponding author.
** Corresponding author at: Department of Materials Science and Engineering, Massachusetts Institute of Technology, Cambridge, MA 02139, United States.
E-mail addresses: gougaoyang@mail.xjtu.edu.cn (G. Gou), liju@mit.edu (J. Li).

http://dx.doi.org/10.1016/j.nanoen.2016.02.036

compounds as semiconducting FE–PV materials. Wide band gaps of ferroelectric oxides result from the large electronegativity difference between metals and oxygen [10]. Compared with oxides, other perovskite systems, such as perovskite sulfides containing the less electronegative sulfur atoms should have smaller E_g. In fact, semiconducting perovskite sulfides have been experimentally synthesized and theoretically predicted [20–23], but none of them are reported to be ferroelectric. Thanks to a new mechanism of hybrid improper ferroelectrics (HIF) recently discovered [24–26], there are opportunities to create ferroelectric perovskite sulfides. Typically, in a paraelectric ABX_3 perovskites with orthorhombic *Pnma* symmetry, there exist $a^-a^-c^0$ and $a^0a^0c^+$ octahedra rotation modes. These two coupled modes can induce non-zero ferroelectric polarization, known as HIF, in layered Ruddlesden–Popper $A_3B_2X_7$ perovskites. Such rotation-driven ferroelectricity have been theoretically predicted [25,27] and then experimentally realized in various Ruddlesden–Popper perovskites [28–31]. As *Pnma* perovskite sulfides ABS_3 already exist in nature [32], once crystalized in Ruddlesden–Popper $A_3B_2S_7$ phase, they can be novel ferroelectrics with diverse functionalities. Without introducing doped cations or non-stoichiometric defects, these stoichiometric single-phase Ruddlesden–Popper ferroelectric sulfides can be promising FE–PV materials, as they potentially have good carrier transport properties as stoichiometric compounds, and large absorption of visible light due to direct band gap [23]. Moreover, the design strategy we proposed should be transferable to other non-polar orthorhombic perovskites, such *Pnma* halide perovskite $CsSnI_3$ [33,34].

Our paper is organized as follows: we start with experimental *Pnma* perovskite sulfides ABS_3 and investigate their octahedral rotation patterns. We then extend to Ruddlesden–Popper $A_3B_2S_7$ sulfides and examine how ferroelectricity is induced by coupled octahedral rotation modes. Electronic structures and optical absorption properties of Ruddlesden–Popper $A_3B_2S_7$ will also be computed. Based on our simulations, ferroelectric sulfides with optimized E_g and electric polarizations can be obtained. Finally, we will discuss the possible experimental synthesis of ferroelectric sulfides.

2. Computational methods

Our first-principles calculations are performed within density-functional theory as implemented in the QUANTUM ESPRESSO code (QE) [35] and the Vienna ab initio Simulation Package (VASP) [36,37]. For calculations within QE code, we use the nonlocal optimized norm-conserving pseudopotentials [38,39] and a 60 Ry plane-wave energy cutoff. PBEsol exchange-correlation functional [40] is used for the calculations, as it can provide improved structural results for pervoskite systems [41,42]. $8 \times 8 \times 6$ and $8 \times 8 \times 4$ Monkhorst–Pack **k**-grids [43] are used to simulate *Pnma* ABS_3 and Ruddlesden–Popper $A_3B_2S_7$ perovskite sulfides respectively. Stable ABS_3 and $A_3B_2S_7$ phases are obtained by performing structural relaxations on soft-mode generated structures until the Hellmann–Feynman forces for each atom is less than 0.1 meV/Å and the stresses less than 0.1 kbar. Soft-mode frequencies and eigen-vectors are calculated based on density functional perturbation theory (DFPT) [44,45]. The electronic contribution to the polarization is calculated following the Berry phase formalism [46].

Using the QE predicted sulfide structures, we further use Heyd–Scuseria–Ernzerhof (HSE) hybrid density functional with screened exact exchange interaction [47,48] implemented in VASP for the electronic structure and optical absorption properties calculations. An energy cutoff of 500 eV and a plane-wave basis set within the projector augmented wave (PAW) [49] method are used for VASP calculations. Spin-orbit coupling (SOC) is excluded in HSE calculations, as the band gap changes due to SOC effect in perovskite sulfides are negligible [23]. It is noted that quasi-particle GW method [50,51] can predict the band gap of a system with better accuracy, but the computational cost for well-converged GW calculations of Ruddlesden–Popper $A_3B_2S_7$ (48 atoms in one unit cell) is unaffordable [23,52]. As a result, HSE hybrid functional calculation becomes an efficient yet accurate approach for electronic structure calculations of perovskite sulfides.

3. Results and discussion

3.1. Structural and ferroelectric properties

Parent ABS_3 perovskite sulfides. Experimentally synthesized ABS_3 perovskite sulfides crystalize in various perovskite phases, which exhibit the corner-, edge- or face-sharing BS_6 octahedra networks [21,32,53,54]. Based on the experimental work of Lelieveld and IJdo [32], we will study the experimental corner-sharing perovskite ABS_3 with A=Ca, Sr and Ba, B=Zr and Hf. These ABS_3 sulfides belong to the orthorhombically distorted perovskite family with the *Pnma* symmetry (No. 62). Our calculated crystal symmetry and lattice parameters agree well with experimental results (Table SI of the supporting information).

As shown in Fig. 1, *Pnma* ABS_3 exhibits $a^-a^-c^0$ and $a^0a^0c^+$ BS_6 octahedra rotations in Glazer notation [55]. Due to the three-dimensional connectivity of the corner-sharing perovskite structure [27,56], octahedra rotations in *Pnma* ABS_3 will also induce the antiferroic distortion (AFD) mode, where A-site cations from two neighboring cation layers are displaced by the same magnitude but along the opposite direction (Fig. 1(b)). As a result, *Pnma* ABS_3 sulfides have zero net polarization.

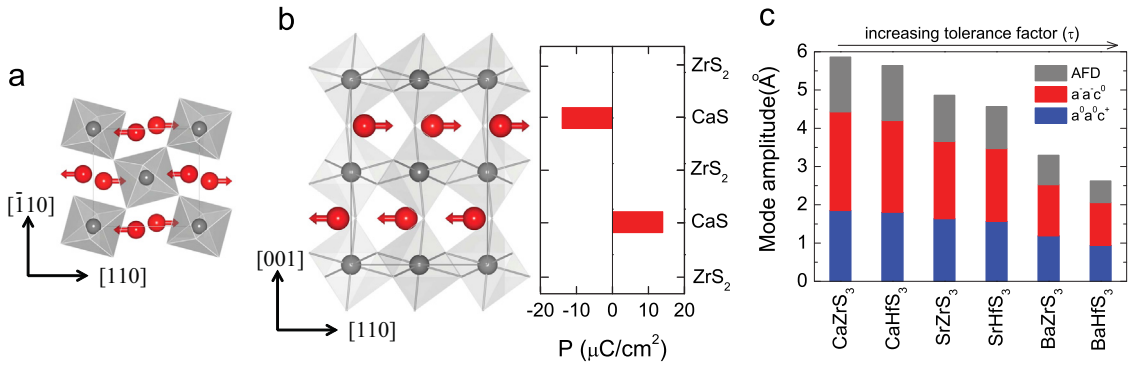

Fig. 1. Atomic structures for *Pnma* corner-sharing ABS_3 (A=Ca, Sr and Ba, B=Zr and Hf). Both top view (a) and side view (b) are shown to emphasize the anti-ferroic distortion (AFD) pattern (A-site cation displacement along pseudo-cubic [110] direction are indicated by arrows). Due to the cancellation of the polarization from each layer (p_{layer}), total polarization $P = \sum p_{layer} = 0$. (c) Amplitudes of the major crystallographic modes in *Pnma* ABS_3 sorted by the tolerance factor.

Similar to perovskite oxides, the magnitudes of structural distortion or rotation of octahedra in ABS_3 sulfides can be characterized by the well-established tolerance factor τ, defined as:

$$\tau \equiv \frac{R_A + R_S}{\sqrt{2}\,(R_B + R_S)} \quad (1)$$

where $(R_A + R_S)$ and $(R_B + R_S)$ correspond to A–S and B–S bond lengths (detailed results in Table SII). For *Pnma* ABS_3 with the pronounced octahedra rotations, their tolerance factors $\tau < 1$. An obvious structural trend is found when we plot the magnitude of crystallographic modes of ABS_3 as a function of the tolerance factor in Fig. 1(c): ABS_3 with smaller tolerance factor (e.g. $CaZrS_3$) has the stronger octahedra rotation magnitudes (larger rotation angles, Fig. S1), and also exhibits the larger anti-ferroic distortion amplitudes. Therefore a question arises: can these octahedral rotations with large amplitudes lead to the enhanced polarization in Ruddlesden–Popper perovskite sulfides?

Ruddlesden–Popper $A_3B_2S_7$ sulfides. With the existence of $a^-a^-c^0$ and $a^0a^0c^+$ octahedra rotations in *Pnma* ABS_3, it is likely to achieve the rotation induced ferroelectricity (HIF) in layered Ruddlesden–Popper perovskites [25,27]. Considering that Ruddlesden–Popper $Ba_3Zr_2S_7$ has already been synthesized experimentally [57,58], we will extend our investigation to Ruddlesden–Popper $A_3B_2S_7$ sulfides derived from the parent *Pnma* ABS_3, and study their rotation induced ferroelectricity.

Ruddlesden–Popper sulfides have the general chemical formula $AS[ABS_3]_n$, where the ABS_3 perovskite blocks (P-blocks) are stacked along [001] direction, inserted by an extra AS layer for every n perovskite units, and inter-layer A cations are coordinated with the terminal S atoms to form rock-salt blocks (R-blocks) [59]. Shown in Fig. 2 are $n=2$ Ruddlesden–Popper $A_3B_2S_7$ sulfide structures. We choose the distortion-free $I4/mmm$ (No. 139) phases as the paraelectric reference for $A_3B_2S_7$, from which the soft phonon modes and corresponding structural instabilities can be identified. Two primary soft modes corresponding to $a^-a^-c^0$ and $a^0a^0c^+$ octahedra rotations are found in $I4/mmm$ phase. After performing structural relaxation on these two soft modes generated structures, ground state Ruddlesden–Popper $A_3B_2S_7$ phases can be obtained.

All of the Ruddlesden–Popper $A_3B_2S_7$ sulfides are optimized to have orthorhombic polar $A2_1am$ (No. 36) symmetry. As shown in Fig. 2, $A_3B_2S_7$ sulfides inherit $a^-a^-c^+$ octahedra rotations from the parent *Pnma* ABS_3. Besides, they also exhibit the spontaneous polarizations along pseudocubic [110] direction. The origin of rotation induced ferroelectricity in $A_3B_2S_7$ can be revealed in cation-layer resolved polarization (p_{layer}) plots (Fig. 2(a) and (b)). Octahedra rotations in orthorhombic $A_3B_2S_7$ also induce AFD-type cation displacement, where A-site cations from the neighboring layers are displaced oppositely. But as octahedra connectivity along [001] direction between different P-blocks are disrupted, in each P-block, two of the three cation-layer dipoles are directed along pseudo-cubic [$\bar{1}$10] direction, while the third is anti-parallel to the others. Therefore, a net polarization arises in Ruddlesden–Popper $A_3B_2S_7$. The polarizations in $A_3B_2S_7$ are mainly contributed by the A-site cation displacement, while the latter depends on the magnitude of the octahedra rotations. It is therefore apparent that $Ca_3Zr_2S_7$ and $Ca_3Hf_2S_7$ with small τ and significant octahedra rotations exhibit large magnitude of polar displacement (Fig. 2(c)).

To quantify the octahedra rotation induced ferroelectricity in Ruddlesden–Popper $A_3B_2S_7$, we further calculate their spontaneous polarizations (P) using the Berry phase method (Fig. 3(a)). By recording the variation of spontaneous polarizations and the total energy of $A_3B_2S_7$ with respect to the change of amplitudes for structural distortion connecting the paraelectric and ferroelectric phases, the typical double-well P–E profiles are obtained (Fig. 3(b)). Two potential wells correspond to two ferroelectric $A_3B_2S_7$ phases of different polarization directions, while the paraelectric state is located at the saddle point. When the potential well gets deep enough, $A_3B_2S_7$ can be stabilized in a stable ferroelectric phase. Therefore, the energetic stability of ferroelectric $A_3B_2S_7$ can be evaluated via ferroelectric stabilization energy ΔE_P, which measures the energy difference between the paraelectric and ferroelectric states. As shown in Fig. 3(a), our calculated P and ΔE_P for $A_3B_2S_7$ decrease continuously as the tolerance factor increases. The extremely small P and ΔE_P in $Ba_3Zr_2S_7$ indicate that it has a very low Curie temperature (T_C) and its ferroelectricity cannot be stable at room temperature, which naturally explains why experimental synthesized $Ba_3Zr_2S_7$ crystalizes in a paraelectric $I4/mmm$ structure [58]. On the other hand, $Ca_3Zr_2S_7$ has a large ΔE_P of 2.5 eV/f.u. *vs.* $\Delta E_P \cong 0.5$ eV/f. u. for Ruddlesden–Popper $Ca_3Ti_2O_7$, whose measured T_C reaches 1100 K [60]. As a result, $Ca_3Zr_2S_7$ should have a stable and experimentally measurable polarization ($P=18.1\ \mu C/cm^2$) at room temperature, which can be an ideal ferroelectric sulfide for experimental study at room temperature and above.

3.2. Electronic structures and optical absorption properties

Non-polar *Pnma* ABS_3 perovskite sulfides can be ferroelectric if they are synthesized in Ruddlesden–Popper $A_3B_2S_7$ structures. To explore the application of ferroelectric $A_3B_2S_7$ as the ferroelectric photovoltaic materials suitable for visible light absorption, their

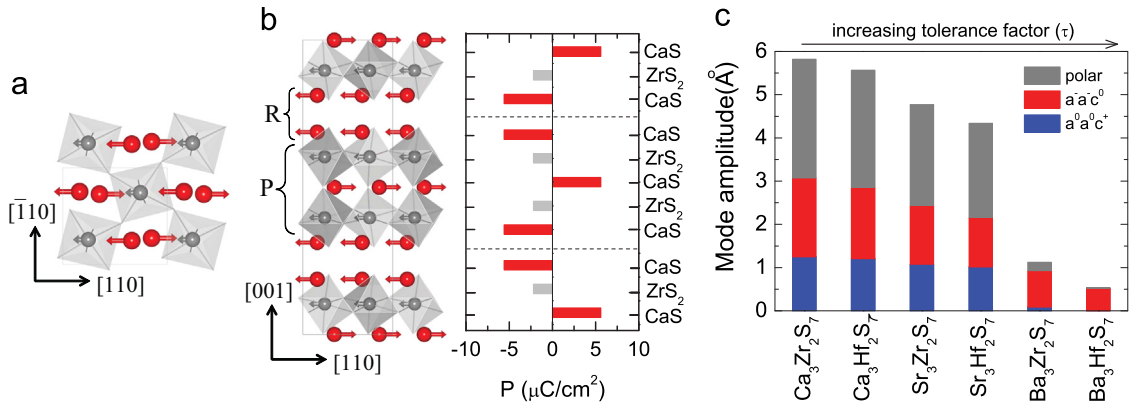

Fig. 2. Crystal structure for Ruddlesden–Popper $A_3B_2S_7$ with the orthorhombic $A2_1am$ symmetry. Top view of perovskite (P) block (a) and side view of both perovskite and rocksalt (R) blocks in $A_3B_2S_7$ are presented. Cation displacement is shown as arrows. $p_{layer} = \Omega^{-1} \cdot \sum_i u_i Z_i^*$, where Ω is the cell volume, u_i is the cation displacement and Z_i^* is the Born effective charge. $\sum p_{layer}$ gives a non-zero total polarization. (c) Amplitudes of $a_+a_+c_0$ polar displacement, $a^-a^-c^0$ and $a^0a^0c^+$ octahedral rotation modes in $A_3B_2S_7$ sorted by the tolerance factor of the parent ABS_3 compounds.

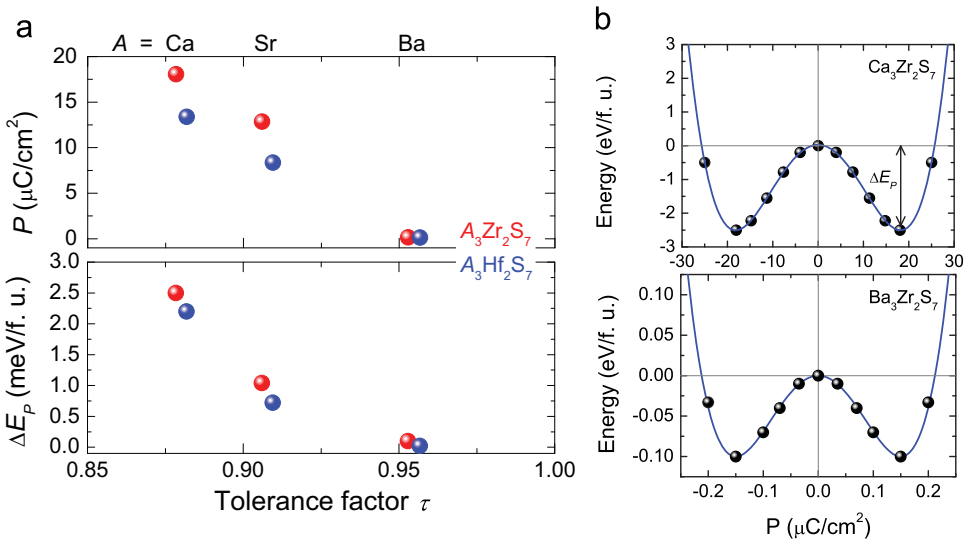

Fig. 3. (a) Spontaneous polarization (P) and ferroelectric stabilization energy (double-well potential depth, ΔE_P) for $A_3B_2S_7$ (A=Ca, Sr and Ba, B=Zr and Hf), sorted by the tolerance factor. (b) Simulated ferroelectric double well potential for $Ca_3Zr_2S_7$ and $Ba_3Zr_2S_7$. Symbols are first-principles results and lines are fitted based on Landau model. $Ca_3Zr_2S_7$ has its P and ΔE_P order of magnitude larger than those in $Ba_3Zr_2S_7$.

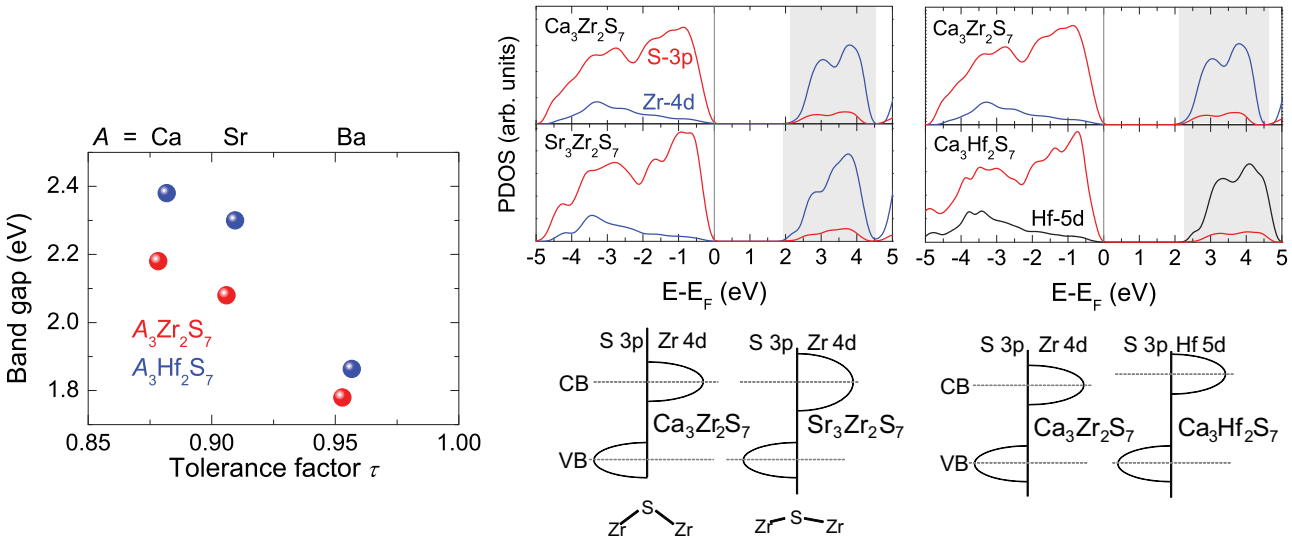

Fig. 4. HSE predicted energy band gaps for Ruddlesden–Popper $A_3B_2S_7$ sorted by perovskite tolerance factor. Comparison of the atom-resolved projected density of states (PDOS) between $Ca_3Zr_2S_7$ and $Sr_3Zr_2S_7$, $Ca_3Zr_2S_7$ and $Ca_3Hf_2S_7$. The conduction states contributed by B-site cation d-orbitals are highlighted as gray areas. Schematic density of state profiles accounting for the band gap difference in $A_3B_2S_7$ are also presented.

electronic structures, especially band gaps (E_g) should be precisely determined. Due to the deficiencies of LDA or GGA method in predicting the energy band gaps, a more accurate HSE hybrid functional [47,48] is used for calculations. HSE calculation provides an accurate prediction of band gaps for perovskite sulfides. For example, HSE predicted band gap for $BaZrS_3$ is only 0.1 eV lower than experimental value [21] (Table SIII).

$A_3B_2S_7$ sulfides are predicted to have direct band gaps within the energy range between 1.8 and 2.4 eV, comparable with medium-bandgap semiconductors such as CdSe and GaP. Besides, *Pnma* ABS_3 sulfides are also predicted to be semiconductors with small E_g (Fig. S2 and Table SIII). The following band gap trends are identified in $A_3B_2S_7$ (Fig. 4): $E_g[A_3Zr_2S_7] < E_g[A_3Hf_2S_7]$, and for each individual $A_3Zr_2S_7$ and $A_3Hf_2S_7$, its E_g decreases monotonically with the tolerance factor. The band gap trend in $A_3B_2S_7$ can be understood from the nature of their electronic structures. Similar to ferroelectric oxides [61], there are pronounced hybridization of electronic states between B-site cations and anions in $A_3B_2S_7$. Typically in $Ca_3Zr_2S_7$, Zr-4d and S-3p states are hybridized/overlapped over the energy range around the Fermi level. The conduction band of the system is mainly contributed by the empty Zr-4d states, while the occupied S-3p states are distributed throughout the entire valence band. Band gap of $Ca_3Zr_2S_7$ refers to the energy difference of band edges between occupied S-3p and empty Zr-4d states.

The electronic structures of $A_3B_2S_7$ are mainly determined by the hybridization/orbital overlap between Zr-4d (Hf-5d) and S-3p states. As shown in Fig. 4, Zr–S orbital overlap will be maximized when Zr–S–Zr bond angle reaches 180°, giving arise to the largest orbital bandwidths. But due to the octahedral rotations, bent Zr–S–Zr bonds in $A_3B_2S_7$ will reduce the magnitude of Zr–S orbital overlap and electronic bandwidths derived from them [62,63]. Therefore, band gap changes in $A_3B_2S_7$ are mediated by the octahedral rotations [64]: compared with $Sr_3Zr_2S_7$, $Ca_3Zr_2S_7$ exhibits larger magnitude of octahedra rotation and smaller orbital band

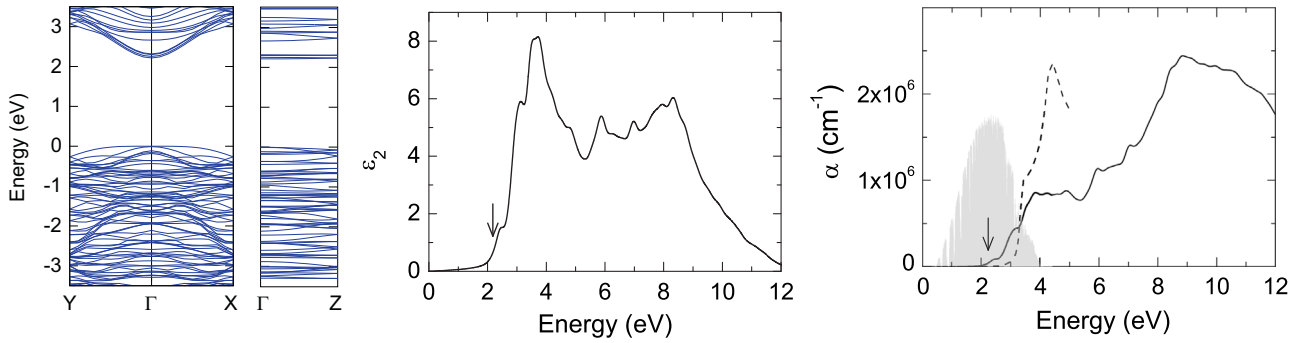

Fig. 5. Band structures, imaginary part of the dielectric function ($\epsilon_2(\omega)$) and absorption coefficient ($\alpha(\omega)$) for ferroelectric $Ca_3Zr_2S_7$, calculated using HSE hybrid functional. $Ca_3Zr_2S_7$ is a direct band gap semiconductor, where both valence band maximum and conduction band minimum are located at Γ point. The arrows mark the position of band gap for $Ca_3Zr_2S_7$. The dash line corresponding to experimental optical absorption coefficient for bulk Si measured at room temperature [67] is used for comparison. The gray area refers to the standard AM 1.5G solar spectrum (in arbitrary units) [68].

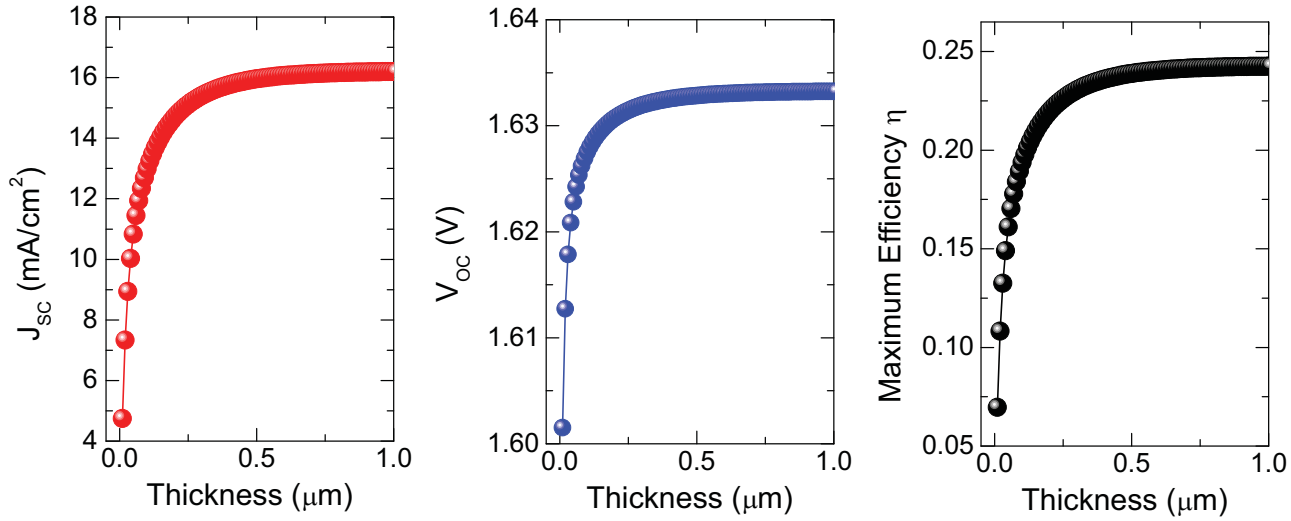

Fig. 6. Our calculated photovoltaic parameters: short-circuit current density J_{sc}, open-circuit voltage V_{oc} and maximum photovoltaic conversion efficiency η for ideal $Ca_3Zr_2S_7$ solar cell, as a function of absorber film thickness.

widths (especially conduction S-3*p*), which finally leads to a larger band gap. Moreover, Hf-5*d* orbital has a higher energy level than Zr-4*d*. After hybridization, Hf-5*d* conduction band will be located at higher energy [65], making $E_g[A_3Hf_2S_7] > E_g[A_3Zr_2S_7]$.

Based on the obtained electronic structures, we further calculate the frequency-dependent dielectric function ($\epsilon(\omega)$) and optical absorption coefficient ($\alpha(\omega)$) of $A_3B_2S_7$. As $Ca_3Zr_2S_7$ exhibits the most stable ferroelectricity and largest spontaneous polarization, we will choose $Ca_3Zr_2S_7$ as a prototype of ferroelectric sulfides for detailed study. ϵ and α are calculated using the independent particle approximation implemented in VASP [66], where many-body effects (e.g. photon-excited excitons) are neglected. Test calculation performed on bulk Si indicates experimental absorption coefficient of Si [67] can be reproduced using the independent particle approximation (Fig. S3).

As shown in Fig. 5, $Ca_3Zr_2S_7$ has a direct band gap of 2.18 eV. Compared with $CaZrS_3$ (band structure shown in Fig. S2) with three-dimensional (3D) corner-sharing octahedra connectivity, 2D layered $Ca_3Zr_2S_7$ only exhibits the largely dispersed energy bands along the in-plane polarization directions (Γ–X and Γ–Y), while the out-of-plane bands along Γ–Z are almost dispersionless.

Our calculated imaginary dielectric function ϵ_2 and absorption coefficient α, that determine the optical absorption properties of $Ca_3Zr_2S_7$ are also given in Fig. 5. Experimental absorption coefficient of Si is also included for comparison. The onset of the optical absorption in $Ca_3Zr_2S_7$ occurs at an energy point exactly same as its fundamental band gap (marked as arrows in Fig. 5), indicating that there is a direct optical transition from valence band maximum to conduction band minimum in $Ca_3Zr_2S_7$. More importantly, within the visible light energy range (photon energy <3.4 eV), $Ca_3Zr_2S_7$ exhibits optical absorption coefficient much larger than that of the single crystal Si (Fig. 5).

3.3. Photovoltaic properties

Ruddlesden–Popper $Ca_3Zr_2S_7$ can effectively absorb visible light with wavelength below 568.7 nm. As the solar spectrum is dominated by visible light, high absorption of visible light is essential for achieving high PV efficiency [69]. To evaluate the photovoltaic performance of $Ca_3Zr_2S_7$ as an ideal solar cell, its PV conversion efficiency needs to be simulated.

PV efficiency of an ideal thin film solar cell can be simulated using the spectroscopic limited maximum efficiency (SLME) method [70]. Such a method takes into account the optical absorption spectrum, energy dependent carrier recombination loss and the thickness of the absorber layer (see supporting information for details). SLME method has been widely and successfully applied for many solar-cell materials, including the perovskites photovoltaic materials [69,71]. Fig. 6 shows our calculated short-circuit current density J_{sc}, open-circuit voltage V_{oc} and maximum photovoltaic efficiency η for $Ca_3Zr_2S_7$, as a function of absorber thickness L. As photo absorptivity increases with the thickness L,

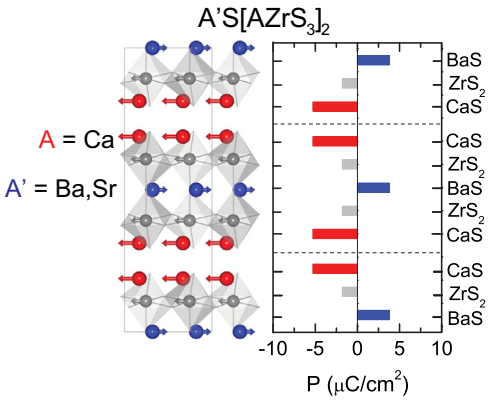

Fig. 7. Crystal structure and cation layered-resolved polarization distribution in *A*-site cation ordered Ruddlesden–Popper $A'S[CaZrS_3]_2$.

Table 1
Calculated averaged perovskite tolerance factor τ_{avg}, ground state total polarization *P*, ferroelectric stabilization energy ΔE_P and band gap E_g for *A*-site cation ordered Ruddlesden–Popper $A'S[CaZrS_3]_2$.

Sulfides	τ_{avg}	P (μC/cm^2)	ΔE_P (eV/f.u.)	E_g (eV)
$CaS[CaZrS_3]_2$	0.878	18.1	2.5	2.18
$SrS[CaZrS_3]_2$	0.888	20.5	1.8	2.11
$BaS[CaZrS_3]_2$	0.903	23.6	1.2	1.98

PV efficiency reaches the maximal value (~ 24%) at large *L*. At a typical absorber thickness of $L=0.5$ μm, the calculated J_{sc} is at the order of mA/cm^2 and efficiency η is about 23%. Such a value is comparable with the calculated PV efficiency for other photovoltaic materials, such as GaAs and $CH_3NH_3PbI_3$ ($\eta \simeq 15\%$ and 23%, when $L=0.5$ μm [69]). The overall good PV performance of $Ca_3Zr_2S_7$ originates from its direct semiconducting band gap and high absorption of visible light [70]. It is worth noting that the experimentally measured efficiency of a solar cell can be affected by many extrinsic effects, such as thin-film preparation, defects, etc. Still our calculated ideal PV properties for $Ca_3Zr_2S_7$ can be a useful guideline for future experimental investigations.

3.4. Extension to cation-ordered Ruddlesden–Popper sulfides

We have shown that Ruddlesden–Popper $Ca_3Zr_2S_7$ with the smallest tolerance factor exhibits the largest polarization and band gap (Figs. 3 and 4) among all $A_3Zr_2S_7$ sulfides we studied. From the experimental point of view, tuning the band gaps of the semiconducting ferroelectric materials will be crucial for optimizing their performance characteristics as solar cells [19]. In this subsection, we will demonstrate the tunability of band gap and ferroelectricity in Ruddlesden–Popper $Ca_3Zr_2S_7$ via *A*-site cation ordering.

Fig. 7 shows the crystal structure for *A*-site ordered Ruddlesden–Popper $A'S[CaZrS_3]_2$ derived from $Ca_3Zr_2S_7$, where Ca cations in the middle of perovskite blocks are substituted by other A' cations with larger radius (A'=Sr and Ba). Compared with pure $Ca_3Zr_2S_7$, electric dipoles from $A'S$ cation layers are smaller, which cannot cancel out with the CaS dipoles [27]. As spontaneous polarization in Ruddlesden–Popper sulfides are mainly contributed by *A*-site cations, *A*-site ordered $(Sr,Ca_2)Zr_2S_7$ and $(Ba,Ca_2)Zr_2S_7$ exhibit enhanced electric polarizations over $Ca_3Zr_2S_7$ (Table 1). Moreover, the ferroelectric stabilization energies ΔE_P in $(Sr,Ca_2)Zr_2S_7$ and $(Ba,Ca_2)Zr_2S_7$ are still large enough to guarantee their ferroelectricity are stable at room temperature. Substitution of Ca by Sr or Ba will also lead to an increase of the average tolerance factor of the system. Based on the τ–E_g relation we established, $A'S[CaZrS_3]_2$ have larger τ_{avg} than $Ca_3Zr_2S_7$ (Table 1), and their band gaps can be further reduced. For example, $(Ba,Ca_2)Zr_2S_7$ has a direct band gap below 2 eV, which can absorb visible light with wavelength below 626.2 nm. Therefore, *A*-site ordered $A'S[CaZrS_3]_2$ have enhanced polarizations and reduced band gaps than pure $Ca_3Zr_2S_7$.

We conclude by providing some guidelines for experimental synthesis of ferroelectric Ruddlesden–Popper sulfides $A_3B_2S_7$ and fabrication of sulfides-based FE-PV devices. Sulfide $Ba_3Zr_2S_7$ in Ruddlesden–Popper structure has been synthesized using solid-state reaction [57] or flux method [58] decades ago. Structural characterization indicates that $Ba_3Zr_2S_7$ has a paraelectric phase with zero polarization. Therefore, ferroelectric properties of perovskite sulfides have never been experimentally explored. Based on our prediction, $Ca_3Zr_2S_7$ has very stable ferroelectricity at room temperature, semiconducting band gap and large optical absorption coefficient. Ferroelectric $Ca_3Zr_2S_7$ could potentially be made using the similar experimental methods for synthesis of $Ba_3Zr_2S_7$, as both $Ca_3Zr_2S_7$ and $Ba_3Zr_2S_7$ are predicted to have the same ground state structure. Moreover, band gaps and ferroelectricity of $Ca_3Zr_2S_7$ can be further tuned via *A*-site cation ordering. Using the modern layer-by-layer thin film deposition techniques [18,24,72], it is possible to prepare *A*-site ordered Ruddlesden–Popper $A'S[CaZrS_3]_2$. Consequently, multilayered ferroelectric thin-film PV device consisting of $Ca_3Zr_2S_7$, $(Sr,Ca_2)Zr_2S_7$ and $(Ba,Ca_2)Zr_2S_7$ single layers can absorb wide range of visible light, and an optimized PV conversion efficiency may be achieved [19].

4. Conclusion

In conclusion, using first-principles calculations, we design a new family of semiconducting perovskite ferroelectrics – Ruddlesden–Popper perovskite sulfides $A_3B_2S_7$, for ferroelectric photovoltaic applications. Especially, Ruddlesden–Popper $Ca_3Zr_2S_7$ is predicted to have the stable ferroelectric polarization which can efficiently separate the photo-generated electron–hole pairs, and low band gap suitable for visible light absorption. Our calculations further demonstrate $Ca_3Zr_2S_7$ as a promising ferroelectric photovoltaic material with the high photovoltaic energy conversion efficiency. Most importantly, Ruddlesden–Popper perovskite sulfides presented in current work can be created by the standard synthesis techniques. We hope our work will motivate the experimental synthesis of ferroelectric perovskite sulfides and exploration of their ferroelectric and photovoltaic properties.

Acknowledgments

The authors acknowledge the funding support from National Basic Research Program of China, under Contract no. 2012CB619402, National Science Foundation of China, under Contract no. 11574244, and Program for Innovative Research Team in University of Ministry of Education of China (IRT13034). J.L. acknowledges support by NSF DMR-1410636. National Supercomputer Center (NSCC) in Tianjin is acknowledged for computational support. The authors thank Prof. Xiaofeng Qian for useful discussion.

Appendix A. Supplementary data

Supplementary data associated with this paper can be found in the online version at http://dx.doi.org/10.1016/j.nanoen.2016.02.036.

References

[1] Y. Yuan, Z. Xiao, B. Yang, J. Huang, J. Mater. Chem. A 2 (2014) 6027–6041.
[2] B. Chen, X. Zheng, M. Yang, Y. Zhou, S. Kundu, J. Shi, K. Zhu, S. Priya, Nano Energy 13 (2015) 582–591.
[3] A.M. Glass, D. von der Linde, T.J. Negran, Appl. Phys. Lett. 25 (1974) 233–235.
[4] S.R. Basu, L.W. Martin, Y.H. Chu, M. Gajek, R. Ramesh, R.C. Rai, X. Xu, J. L. Musfeldt, Appl. Phys. Lett. 92 (2008) 091905.
[5] S.Y. Yang, et al., Appl. Phys. Lett. 95 (2009) 062909.
[6] T. Choi, S. Lee, Y.J. Choi, V. Kiryukhin, S.-W. Cheong, Science 324 (2009) 63–66.
[7] J. Seidel, D. Fu, S.-Y. Yang, E. Alarcón-Lladó, J. Wu, R. Ramesh, J.W. Ager, Phys. Rev. Lett. 107 (2011) 126805.
[8] K. Prashanthi, P. Dhandharia, N. Miriyala, R. Gaikwad, D. Barlage, T. Thundat, Nano Energy 13 (2015) 240–248.
[9] W. Zhang, M.-M. Yang, X. Liang, H.-W. Zheng, Y. Wang, W.-X. Gao, G.-L. Yuan, W.-F. Zhang, X.-G. Li, H.-S. Luo, R.-K. Zheng, Nano Energy 18 (2015) 315–324.
[10] I. Grinberg, D.V. West, M. Torres, G. Gou, D.M. Stein, L. Wu, G. Chen, E.M. Gallo, A.R. Akbashev, P.K. Davies, J.E. Spanier, A.M. Rappe, Nature 503 (2013) 509–512.
[11] S.Y. Yang, J. Seidel, S.J. Byrnes, P. Shafer, C.-H. Yang, M.D. Rossell, P. Yu, Y.-H. Chu, J.F. Scott, J.W. Ager, L.W. Martin, R. Ramesh, Nat. Nanotechnol. 5 (2010) 143–147.
[12] W. Shockley, H.J. Queisser, J. Appl. Phys. 32 (1961) 510–519.
[13] J.W. Bennett, I. Grinberg, A.M. Rappe, J. Am. Chem. Soc. 130 (2008) 17409–17412.
[14] G.Y. Gou, J.W. Bennett, H. Takenaka, A.M. Rappe, Phys. Rev. B 83 (2011) 205115.
[15] R.F. Berger, J.B. Neaton, Phys. Rev. B 86 (2012) 165211.
[16] X.S. Xu, J.F. Ihlefeld, J.H. Lee, O.K. Ezekoye, E. Vlahos, R. Ramesh, V. Gopalan, X.Q. Pan, D.G. Schlom, J.L. Musfeldt, Appl. Phys. Lett. 96 (2010) 192901.
[17] R. Nechache, C. Harnagea, S. Licoccia, E. Traversa, A. Ruediger, A. Pignolet, F. Rosei, Appl. Phys. Lett. 98 (2011) 202902.
[18] W.S. Choi, M.F. Chisholm, D.J. Singh, T. Choi, G.E. Jellison Jr., H.N. Lee, Nat. Commun. 3 (2012) 689.
[19] R. Nechache, C. Harnagea, S. Li, L. Cardenas, W. Huang, J. Chakrabartty, F. Rosei, Nat. Photonics 9 (2015) 61–67.
[20] A. Ishikawa, T. Takata, J.N. Kondo, M. Hara, H. Kobayashi, K. Domen, J. Am. Chem. Soc. 124 (2002) 13547–13553.
[21] W. Meng, B. Saparov, F. Hong, J. Wang, D.B. Mitzi, Y. Yan, Chem. Mater. 28 (2016) 821–829.
[22] J.W. Bennett, I. Grinberg, A.M. Rappe, Phys. Rev. B 79 (2009) 235115.
[23] Y.-Y. Sun, M.L. Agiorgousis, P. Zhang, S. Zhang, Nano Lett. 15 (2015) 581–585.
[24] E. Bousquet, M. Dawber, N. Stucki, C. Lichtensteiger, P. Hermet, S. Gariglio, J.-M. Triscone, P. Ghosez, Nature 452 (2008) 732–736.
[25] N.A. Benedek, C.J. Fennie, Phys. Rev. Lett. 106 (2011) 107204.
[26] J.M. Rondinelli, C.J. Fennie, Adv. Mater. 24 (2012) 1961–1968.
[27] A.T. Mulder, N.A. Benedek, J.M. Rondinelli, C.J. Fennie, Adv. Funct. Mater. 23 (2013) 4810–4820.
[28] M.S. Senn, A. Bombardi, C.A. Murray, C. Vecchini, A. Scherillo, X. Luo, S. W. Cheong, Phys. Rev. Lett. 114 (2015) 035701.
[29] Y.S. Oh, X. Luo, F.-T. Huang, Y. Wang, S.-W. Cheong, Nat. Mater. 14 (2015) 407–413.
[30] H. Akamatsu, K. Fujita, T. Kuge, A. Sen Gupta, A. Togo, S. Lei, F. Xue, G. Stone, J.M. Rondinelli, L.-Q. Chen, I. Tanaka, V. Gopalan, K. Tanaka, Phys. Rev. Lett. 112 (2014) 187602.
[31] M.J. Pitcher, P. Mandal, M.S. Dyer, J. Alaria, P. Borisov, H. Niu, J.B. Claridge, M.J. Rosseinsky, Science 347 (2015) 420–424.
[32] R. Lelieveld, D.J.W. IJdo, Acta Crystallogr. Sect. B 36 (1980) 2223–2226.
[33] I. Chung, B. Lee, J. He, R.P.H. Chang, M.G. Kanatzidis, Nature 485 (2012) 486.
[34] I. Chung, J.-H. Song, J. Im, J. Androulakis, C.D. Malliakas, H. Li, A.J. Freeman, J.T. Kenney, M.G. Kanatzidis, J. Am. Chem. Soc. 134 (2012) 8579–8587.
[35] P. Giannozzi, et al., J. Phys.: Condens. Matter 21 (2009) 395502.
[36] G. Kresse, J. Furthmüller, Phys. Rev. B 54 (1996) 11169–11186.
[37] G. Kresse, D. Joubert, Phys. Rev. B 59 (1999) 1758–1775.
[38] A.M. Rappe, K.M. Rabe, E. Kaxiras, J.D. Joannopoulos, Phys. Rev. B 41 (1990) 1227–1230.
[39] N.J. Ramer, A.M. Rappe, Phys. Rev. B 59 (1999) 12471–12478.
[40] J.P. Perdew, A. Ruzsinszky, G.I. Csonka, O.A. Vydrov, G.E. Scuseria, L. A. Constantin, X. Zhou, K. Burke, Phys. Rev. Lett. 100 (2008) 136406.
[41] R. Wahl, D. Vogtenhuber, G. Kresse, Phys. Rev. B 78 (2008) 104116.
[42] G. Gou, J.M. Rondinelli, Adv. Mater. Interfaces 1 (2014) 1400042.
[43] H.J. Monkhorst, J.D. Pack, Phys. Rev. B 13 (1976) 5188–5192.
[44] S. Baroni, S. De Gironcoli, A.D. Corso, Rev. Mod. Phys. 73 (2001) 515–562.
[45] X. Gonze, Phys. Rev. A 52 (1995) 1096–1114.
[46] R.D. King-Smith, D. Vanderbilt, Phys. Rev. B 47 (1993) 1651–1654.
[47] J. Heyd, G.E. Scuseria, M. Ernzerhof, J. Chem. Phys. 118 (2003) 8207–8215.
[48] J. Heyd, G.E. Scuseria, M. Ernzerhof, J. Chem. Phys. 124 (2006) 219906.
[49] P.E. Blöchl, Phys. Rev. B 50 (1994) 17953–17979.
[50] M.S. Hybertsen, S.G. Louie, Phys. Rev. Lett. 55 (1985) 1418–1421.
[51] M.S. Hybertsen, S.G. Louie, Phys. Rev. B 34 (1986) 5390–5413.
[52] X. Qian, P. Umari, N. Marzari, Phys. Rev. B 84 (2011) 075103.
[53] C.-S. Lee, K.M. Kleinke, H. Kleinke, Solid State Sci. 7 (2005) 1049–1054.
[54] M. Ghedira, J. Chenavas, F. Sayetat, M. Marezio, O. Massenet, J. Mercier, Acta Crystallogr. Sect. B 37 (1981) 1491–1496.
[55] A.M. Glazer, Acta Crystallogr. Sect. B 28 (1972) 3384–3392.
[56] N.A. Benedek, A.T. Mulder, C.J. Fennie, J. Solid State Chem. 195 (2012) 11–20.
[57] M. Saeki, Y. Yajima, M. Onoda, J. Solid State Chem. 92 (1991) 286–294.
[58] B.-H. Chen, B. Eichhorn, W. Wong-Ng, Acta Crystallogr. Sect. C 50 (1994) 161–164.
[59] S.N. Ruddlesden, P. Popper, Acta Crystallogr. 11 (1958) 54–55.
[60] X.Q. Liu, J.W. Wu, X.X. Shi, H.J. Zhao, H.Y. Zhou, R.H. Qiu, W.Q. Zhang, X.M. Chen, Appl. Phys. Lett. 106 (2015) 202903.
[61] R.E. Cohen, Nature 358 (1992) 136–138.
[62] J.B. Torrance, P. Lacorre, A.I. Nazzal, E.J. Ansaldo, C. Niedermayer, Phys. Rev. B 45 (1992) 8209–8212.
[63] G. Gou, I. Grinberg, A.M. Rappe, J.M. Rondinelli, Phys. Rev. B 84 (2011) 144101.
[64] J.M. Rondinelli, S.J. May, J.W. Freeland, MRS Bull. 37 (2012) 261–270.
[65] E.G. Rogers, P. Dorenbos, ECS J. Solid State Sci. Technol. 3 (2014) 173–184.
[66] M. Gajdoš, K. Hummer, G. Kresse, J. Furthmüller, F. Bechstedt, Phys. Rev. B 73 (2006) 045112.
[67] M.A. Green, M.J. Keevers, Prog. Photovolt.: Res. Appl. 3 (1995) 189–192.
[68] ⟨http://rredc.nrel.gov/solar/spectra/am1.5/⟩.
[69] W.-J. Yin, T. Shi, Y. Yan, Adv. Mater. 26 (2014) 4653–4658.
[70] L. Yu, A. Zunger, Phys. Rev. Lett. 108 (2012) 068701.
[71] X. Huang, T.R. Paudel, S. Dong, E.Y. Tsymbal, Phys. Rev. B 92 (2015) 125201.
[72] P. Zubko, S. Gariglio, M. Gabay, P. Ghosez, J.-M. Triscone, Annu. Rev. Condens. Matter Phys. 2 (2011) 141–165.

Hua Wang received his B.S. degree in Nuclear Engineering from Xi'an Jiaotong University in 2012 and M. S. degree in Condensed Matter Physics from Xi'an Jiaotong University in 2015. He is currently a Ph.D. Student in the Department of Materials Science and Engineering at Taxes A&M University. His research mainly focuses on first-principles calculation of novel energy materials.

Gaoyang Gou is an Assistant Professor in Frontier Institute of Science and Technology in Xi'an Jiaotong University. Prior to this appointment, Dr. Gou was postdoctoral research fellow at the Department of Chemistry, University of Pennsylvania from 2009 to 2011. He received his Ph.D. degree in Condensed Matter Physics at the University of Science and Technology of China in 2009 and B.S. degree at University of Science and Technology of China in 2004. His current research focuses on first-principles study of the basic mechanism underlying ferroic perovskite behavior as well as designing new functional ferroic materials for energy applications.

Ju Li is BEA Professor of Nuclear Science and Engineering and Professor of Materials Science and Engineering at MIT. His group (http://Li.mit.edu) performs computational and experimental research on mechanical properties of materials, and energy storage and conversion. Ju obtained a Ph.D. degree in Nuclear Engineering from MIT in 2000, and Bachelor's degree in Physics from University of Science and Technology of China in 1994. He is a recipient of the 2005 Presidential Early Career Award for Scientists and Engineers, 2006 MRS Outstanding Young Investigator Award, and 2007 TR35 award from Technology Review magazine. Thomson Reuters included Ju in its Highly Cited Researchers list in 2014, among 147 scientists world-wide in the Materials Science category. Ju was elected Fellow of the American Physical Society in 2014.